Research Article

Developing synthetic sandstones using geopolymer binder for constraining coupled processes in porous rocks

Markus Peltz[1] · Laurence Warr[1] · Sina Hale[2] · Philipp Blum[2]

Abstract

There is a current need for developing improved synthetic porous materials for better constraining the dynamic and coupled processes relevant to the geotechnical use of underground reservoirs. In this study, a low temperature preparation method for making synthetic rocks is presented that uses a geopolymer binder cured at 80 °C based on alkali-activated metakaolin. For the synthesised sandstone, the key rock properties permeability, porosity, compressive strength, and mineralogical composition, are determined and compared against two natural reservoir rocks. In addition, the homogeneity of the material is analysed structurally by micro-computed tomography and high-resolution scanning electron microscopy, and chemically by energy dispersive X-ray spectroscopy. It is shown that simple, homogenous sandstone analogues can be prepared that show permeability-porosity values in the range of porous reservoir rocks. The advance in using geopolymer binders to prepare synthetic sandstones containing thermally sensitive minerals provides materials that can be easily adapted to specific experimental needs. The use of such material in flow-through experiments is expected to help bridge the gap between experimental observations and numerical simulations, leading to a more systematic understanding of the physio-chemical behaviour of porous reservoir rocks.

Article highlights

- A novel approach for developing synthetic sandstones at low temperatures using geopolymer binder is presented.
- A variety of material properties can be easily controlled which allows adaption to attain specific experimental requirements.
- Geopolymer-bound synthetic sandstones are an ideal material for studying thermally sensitive materials such as carbonates in reactive flow-through experiments.

✉ Markus Peltz, markus.peltz@uni-greifswald.de; ✉ Laurence Warr, warr@uni-greifswald.de | [1]Institute of Geography and Geology, University of Greifswald, 17489 Greifswald, Germany. [2]Institute of Applied Geosciences (AGW), Karlsruhe Institute of Technology (KIT), 76131 Karlsruhe, Germany.

1 Introduction

Quantifying and modelling the processes of fluid-rock interaction in geological reservoir rocks related to the extraction or storage of georesources are an important part of effectively using Earth's upper crustal resources with minimal detriment to the environment. Reservoir rocks located close to the surface, which hold 99% of all freshwater, are increasingly impacted by the accumulation of groundwater pollutants [1, 2]. At greater depths, geological reservoir formations still host significant hydrocarbon reserves in the form of oil or methane gas that continue to provide the main source of global energy through the burning of these fossil fuels. These very same reservoirs can be used to store CO_2 as part of a carbon capture and storage (CCS) approach that is still in the process of upscaling and finding social acceptance [3]. In the quest to move away from fossil fuel dependence, geological reservoirs may also represent suitable places for the seasonal storage of renewable energy gases, such as CH_4 and/or H_2 [4], as well as provide temporary retention sites for heat [5]. Such applications are additional to the current extraction of natural geothermal energy from reservoirs characterised by high thermal gradients and enhanced levels of heat flow [6].

One of the main limitations in advancing the geological engineering of injection or extraction procedures is the difficulty in quantifying the coupled processes that occur during fluid-rock interactions in these complex natural reservoir systems [7, 8]. Porous and tight reservoir sandstones, for example, normally contain several types of minerals present in the form of detrital clasts, diagenetically formed cements or more loosely held pore-filling mineral particles. These develop during the long and complex histories of geological reservoir rocks that include sedimentation, burial diagenesis and subsequent stages of alteration related to fluid-rock interaction and rock deformation [9]. As a result, reservoir rocks are rarely simple but instead represent poly-mineralic assemblages of detrital and authigenic components that are heterogeneous on a multitude of scales, both compositionally and texturally. Such sedimentary and diagenetic variations are observable at the sub-micrometre scale as well as on the centimetre to meter scale [10].

Reservoir sandstone heterogeneities also include multiple generations of similar minerals, such as different types of carbonates, zeolites and clay minerals, which form under low temperature conditions and are often present in the same natural sample [11, 12]. These minerals commonly display diverse varieties of diagenetic textures representative of complex fluid flow behaviour, dissolution and precipitation reactions, as well as particle mobilisation and pore space modifications [13]. In the case of the formation of illite, which is a clay mineral common to sandstone reservoirs subjected to the circulation of potassium-bearing fluids, crystals of varying shape and size may form as platy grain coatings by direct replacement reactions of K-feldspar grains or as fibrous crystals that grow into the open pore space [12]. In these cases, the more complex the rock, the more challenging it becomes to understand and predict its behaviour under varying chemical and hydraulic conditions, such as the changes in porosity and permeability commonly experienced during natural water circulation. These complexities are also evident in experimental flow-through experiments conducted using natural porous rocks, where complex flow patterns, low accessible surface areas and time-dependent dynamic variations limit the applicability of reactive transport modelling [14, 15]. When models can be applied, their validation is often characterised by inconsistent results [16].

As reservoir sandstones are often too complex to easily constrain specific processes, different methods of synthesising simpler rock assemblages have been attempted [17–20]. Early studies utilised epoxy resin, which resulted in good cementation but provided a poor natural analogue [17]. Other techniques used sintered glass beads [19] or 3D-printed models [21] to successfully study particle transport and multi-phase flow in porous media. Another approach to mimic quartz cementation was to use sodium silicate solution as a binder [18, 22, 23], but this technique required rather high temperatures (> 600 °C) to produce a sufficiently strong silicate cementation [24]. Tillotson et al. [20] found that the strength of a synthetic rock can be further increased by adding kaolinite to the sodium silicate—sand mixture, which was subsequently heated beyond the dehydroxylation temperature of kaolinite during the hardening process.

One type of binder that does not require a high curing temperature are geopolymers. These are based on dehydroxylated Al- and Si-rich precursor materials, such as metakaolin, coal fly ash or ground blast furnace slag [25]. After alkali-activation, which involves the dissolution of precursor materials in concentrated NaOH or KOH solutions and the subsequent alkaline hydrolysis of the dissolved Al and Si species, low temperature curing occurs through a series of polymerisation and condensation reactions [26, 27]. In these polymer structures, alkali metal cations have a stabilising effect by compensating charge imbalances. As a consequence, binders containing amorphous geopolymer and crystalline zeolite form at temperatures < 100 °C [28, 29].

As part of recent research activities in studying the complex reactions kinetics of calcite dissolution coupled with the mobilisation of clay minerals in natural reservoir

sandstones [15], there has emerged a clear necessity for developing simpler synthetic analogues for constraining otherwise difficult to resolve coupled processes. To achieve this, the present study outlines a novel approach of preparing synthetic rocks utilising an alkali-activated metakaolin-based geopolymer binder cured at 80 °C that allows thermally sensitive minerals, such as calcite or clay minerals, to be included. Based on quantitative X-ray diffraction analyses and detailed SEM-EDX observations, it is shown that a synthetic calcite-bearing sandstone can be prepared with a binder composed of amorphous geopolymer and crystalline zeolite. Measurements of porosity, permeability and compressive strength paired with computed tomography analyses and direct numerical simulations reveal that the proposed preparation method can be used to produce a synthetic sandstone with petrophysical values in the range of natural reservoir rocks, although improvements are still required to enhance the materials compressive strength. Based on this reaction system, we provide an outlook for potential applications of this type of synthetic rock by outlining the range of parameters that can be adjusted during sample preparation for the purpose of constraining coupled reservoir-relevant properties.

When used in the present article, the term cement refers to its geologic meaning as a lithifying agent rather than to a specific type of limestone-based binder, such as Portland cement.

2 Materials and methods

2.1 Sample preparation

An illustration of the workflow employed to prepare the geopolymer-based synthetic sandstone under low temperature conditions is shown in Fig. 1a and b. The kaolin used was a well crystalline China Clay variety referred to as SPS (selected particle size) from Cornwall, UK. Based on X-ray diffraction analyses (XRD) and Rietveld refinement using the software Profex [30] it contains by weight 96.4% kaolinite, 3.2% muscovite and 0.4% of quartz. This sample, which was obtained from the University of Greifswald collection (TS number 809) was placed in a ceramic tray and heated at 600 °C for 3 h. The heat-treated powder was then cooled to laboratory conditions and subsequently ground for 30 min using an agate ball mill. The amorphous state of the metakaolin powder was confirmed by XRD by the absence of kaolinite reflections and the formation of a characteristic elevated background between 15° and 40° 2θ (Fig. 2). The amorphous XRD pattern is very similar to other metakaolin powders reported in the literature [31]. For the framework grains, a commercially available sea sand (Carl Roth, No. 8441, extra pure, < 250 μm) was used. Its purity (> 99.6% quartz with traces of titanium oxides) was confirmed

by powder XRD and Rietveld analysis. For the preparation of a pure calcite source, a single large Iceland Spar crystal was crushed and ground to obtain a 63–250 μm size fraction by sieving. Based on XRD analysis and quantification it was found to consist of 99.7% calcite and 0.3% of quartz that was probably introduced during grinding.

The binder was prepared by mixing 25% NaOH (6.25 M) solution (Carl Roth, No. 4351, extra pure) and sodium silicate solution (VWR, No. 28079.320, technical grade) with metakaolin in a weight ratio of 2.5:2.5:1. This corresponds to a Si/Al molar ratio of 2.2, which is in the range of well accepted ratios for the production of geopolymers from metakaolin with high compressive strengths and short curing times [e.g. 32, 33]. Following initial tests, a specific order of mixing was adopted in order to maximise the hardening of the binder and better mimic the textures of natural sandstones. First, the metakaolin was mixed with NaOH and hand-stirred until the mixture was homogenised. This step enhanced initial dissolution of Al and Si from the powder, which is required for the subsequent condensation of Al-Si polymers. As a high 6.25 M concentration of NaOH was used, this stage of dissolution is considered to be stoichiometric and thus release similar concentrations of both Al and Si. Second, the sodium silicate solution was added to the binder and homogenised using a planetary centrifugal mixer (Thinky U.S.A. Inc., USA) for 2 min at 2000 rpm. This step adds additional reactive Si to enhance hardening during the condensation and precipitation process. Without time delay, the sea sand was then added and carefully stirred by hand until the quartz grains were evenly coated. Calcite, as an exemplary reactive component, was added during the last stage of preparation to prevent calcite grains from being excessively coated by the binder. The amount of calcite was chosen so that its dissolution during reactive transport experiments would not lead to structural instabilities.

The pre-cured mixture was calculated to contain by weight 85% quartz, 10% calcite and 5% metakaolin when only the dry components are considered. This is equivalent to 70.8% quartz, 8.3% calcite and 20.8% metakaolin binder by weight when the NaOH and sodium silicate solution are considered. For curing, the sandstone mixture was placed into cylindrical molds of either 15 or 25 mm in diameter and heated in a desiccator at 80 °C for 7 days, which was found to be the minimum time required to complete the geopolymerisation reaction. This time is consistent with values reported in literature [e.g. 29]. The bottom of the desiccator was filled with water, but the valve remained open for water to evaporate. This allowed the samples to slowly dry, which enhanced the strength of the sample material during the curing process and prevented the formation of drying cracks. While some water is required to facilitate the geopolymerisation reaction during curing, too much water
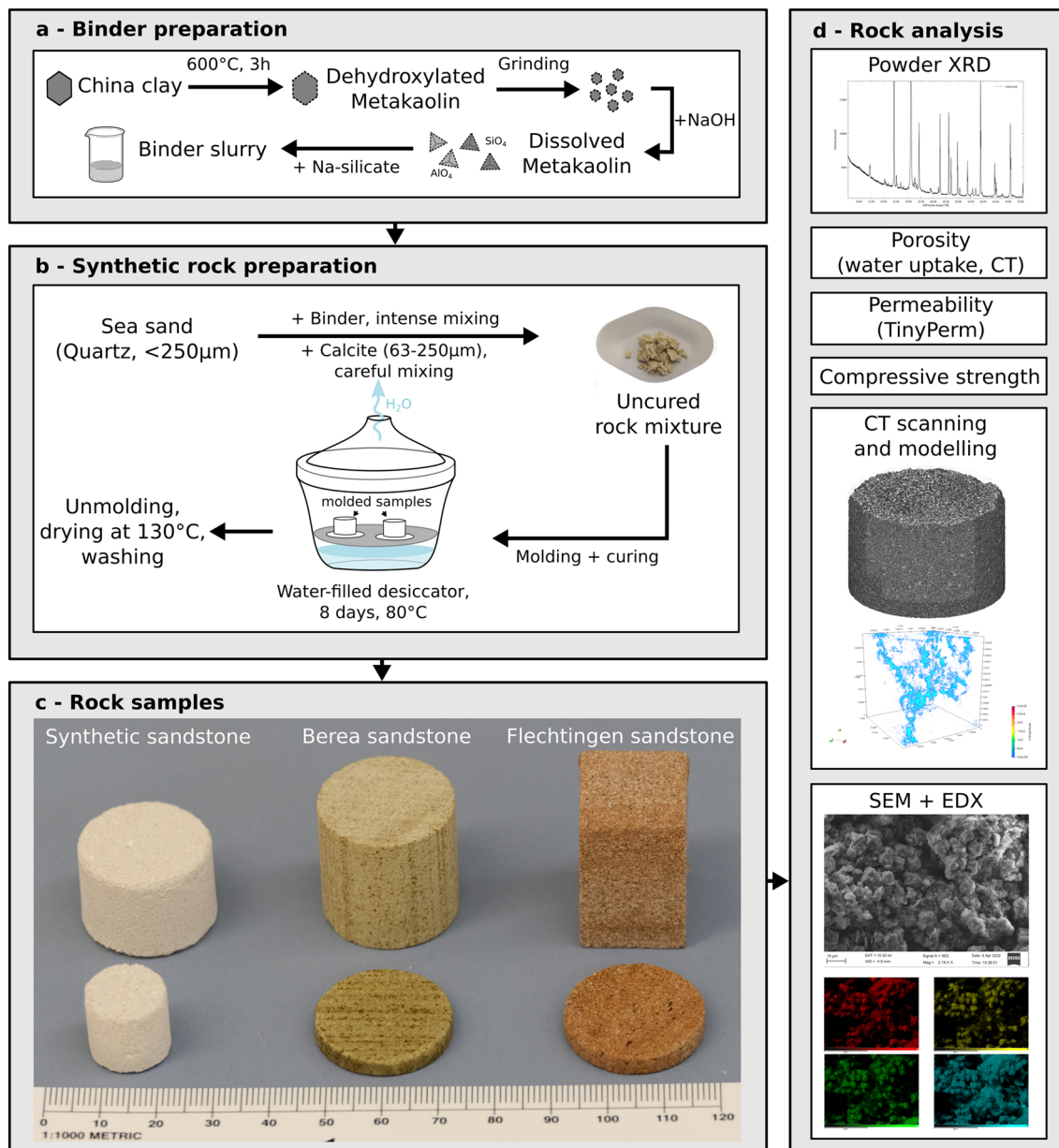
Fig. 1 **a + b** Schematic illustration of the workflow applied for the preparation of the binder and the synthetic rock. **c** Photographs of the synthetic sandstone sample and core samples of the Berea and Flechtingen sandstone. **d** Overview of analytical methods used to study the synthetic sandstone

can lead to dilution of the reacting alkaline solution and to the inhibition of the condensation and precipitation process [34]. Afterwards, samples were removed from the molds and dried in an oven at 130 °C for another 3 days. This latter step may not always be required, but for the material prepared in this study this step was seen to further enhance compressive strength. The final stage of preparation involved removal of any unreacted NaOH from the cured samples by washing in double-distilled water. The water was exchanged until the pH in the beaker approached that of the double-distilled water (pH 5.2). This procedure represents an important step

to test the success of the geopolymer binder as insufficient reaction will lead to materials that soften and breakup during final washing.

2.2 Analytical methods and sample characterisation

2.2.1 X-ray diffraction (XRD)

The mineralogical compositions of the starting materials and the synthetic sandstone were analysed using powder
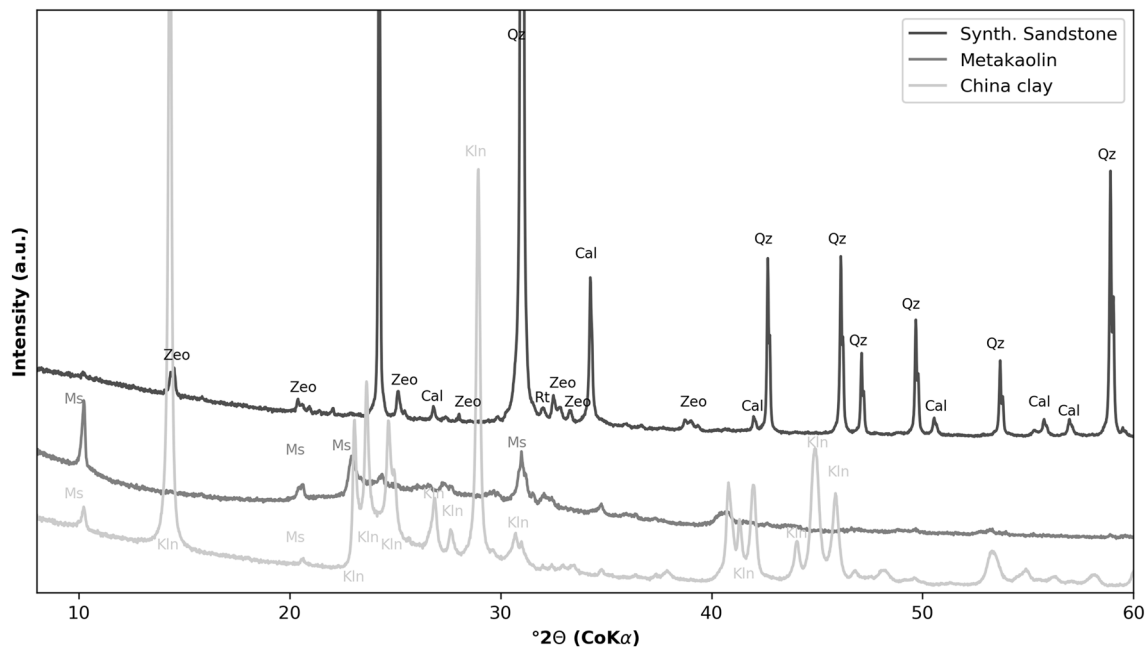
Fig. 2 X-ray diffraction patterns of the initial China clay, metakaolin after heating at 600 °C for 2 h and the micronised synthetic sandstone. (*Ms* muscovite, *Kln* kaolinite, *Qz* quartz, *Cal* calcite, *Zeo* zeolite, *a.u.* arbitrary unit)

X-ray diffraction (XRD) and Rietveld calculations. XRD patterns were measured between 3° and 80° 2θ at 1° 2θ/min using a Bruker D8 Advance diffractometer (Karlsruhe, Germany) equipped with a Lynxeye 1D stripe detector and CoKα radiation at 40 kV and 30 mA. The divergence slit was set to an opening angle of 0.5°. All samples were ground and micronised prior to the preparation of side-loaded random powders. Data was analysed using the Diffrac. EVA software (Bruker, Germany) and the PDF2.0 database. Quantification of mineral components was undertaken using Profex [30].

2.2.2 Scanning electron microscopy (SEM)

The top and bottom Pd-coated surfaces of the samples were analysed using a Zeiss Auriga (Oberkochen, Germany) field emission scanning electron microscope (SEM) operated at 15 kV and images were collected using a secondary electron Everhart-Thornley-style detector. Energy dispersive X-ray spectroscopy (EDX) was carried out at 15 kV using an Oxford X-MAX 80 mm^2 detector (Wiesbaden, Germany) to determine the chemical composition of the binder. Input count rates were limited to 25,000 counts per second. Spot measurements of varying rectangular size were limited by a count integral of 500,000 total counts. EDX mappings were collected at an image resolution of 512 × 384, a dwell time of 100 µs per pixel and with total of 20 overlain maps.

2.2.3 Permeability

The air permeability of the sample plugs was measured with the transient-flow air permeameter *TinyPerm 3* (New England Research, Inc., USA). A detailed description of the process is given in Hale et al. [35] and Hale and Blum [36].

2.2.4 Compressive strength

Uniaxial compressive strength values were approximated using a calibrated inhouse device made of a torque wrench attached to a screw clamp. A detailed description of this measurement method and calibration curves against DIN EN 12390-3 normal procedures are given in Dietel et al. [37].

2.2.5 Computed tomography (CT) and modelling

Computed tomography (CT) imaging was used to determine the porosity and microstructure of a 15 mm synthetic sandstone sample plug. Measurements were run on a YXLON CT Precision system housed at the Institute of Applied Materials—Materials Science and Engineering of the Karlsruhe Institute of Technology [38, 39]. In total, 1950 projections were acquired for the CT scan. The reconstructed dataset had a voxel size of 7.6 µm. Image processing was done using the software Avizo 9.0 (FEI, Germany) and included non-local means filtering to remove noise, ring artifact removal and cropping to a rectangular

domain (x = 1300, y = 1229, z = 1300). Five phases were distinguishable after filtering, namely pores, quartz, calcite, binder and minor amounts of titanium oxide, which showed the highest degree of X-ray absorption. These were segmented using the machine-learning software Ilastik [40]. For every 200th image, a manually formed segmentation mask was created as a training data set. The obtained phase image was statistically analysed using Avizo. Pore and binder size distributions were calculated based on the algorithm proposed by Münch and Holzer [41]. For comparison, a 25 mm Berea sandstone plug was scanned with a voxel size of 13.3 µm.

Subdomains of 384^3 voxels were used for direct numerical simulations by applying the OpenFOAM toolbox [42] to calculate the permeability of the material and analyse the flow path distribution. The SimpleFOAM solver, which uses the SIMPLE algorithm (Semi-Implicit Method for Pressure-Linked Equations) was utilised to solve the Navier–Stokes equations. For laminar flow of incompressible fluids, the conservation of mass is

$$\nabla \cdot v = 0 \,, \tag{1}$$

where v is the divergence-free velocity. The momentum equation without gravitational term reads

$$\mu \nabla^2 v = \rho \left(\frac{\partial v}{\partial t} + v \cdot \nabla v \right) + \nabla p, \tag{2}$$

where μ is the dynamic fluid viscosity, ρ the density of the fluid and p the pressure field.

The mesh was generated to be congruent with a segmented connected pore voxel volume. A single-layer mesh refinement was performed at the boundary of the pore space to prevent an under-resolved mesh in the narrow pore throat regions. Between the inflow and outflow planes, which were enlarged by 10 cells as a "reservoir" in each direction, a constant pressure gradient was adopted. No slip boundary conditions were used for solid grain boundaries and symmetric boundaries were applied for the remaining domain sites. Fluid properties were set to mimic air at 21 °C. Simulations were run in the y-direction, equivalent to the direction of air permeameter measurements. To determine the permeability for each subdomain, the velocity u_y of the computed velocity field was integrated over the sample volume V without reservoirs and the absolute permeability was calculated as follows:

$$K_y = -\mu \left(\frac{1}{V} \int_V u_y dV \left(\frac{\Delta P}{l_y} \right)^{-1} \right), \tag{3}$$

where K_y is the permeability in y-direction, μ is the dynamic viscosity, ΔP the pressure gradient between inflow and

outflow plane and l_y length of the domain in y-direction without reservoirs.

3 Results and discussion

3.1 Mineralogical composition

The XRD pattern of the cured synthetic sample after crushing and micronising was compared to the initial China clay and the metakaolin pattern (Fig. 2). Reflections of quartz, calcite and crystalline zeolite (likely zeolite NaP of the gismondine framework [43] or phillipsite) were observed. Traces of muscovite can be recognised by a tiny 10 Å reflection. No amorphous hump was detected in the cured sandstone sample, as detected in the original metakaolin sample, indicating close to complete dissolution of the amorphous precursor material. Based on Rietveld calculations, the cured synthetic sandstone is composed of 84 wt% quartz, 8 wt% calcite, 6 wt% zeolite and traces of muscovite and titanium oxides (Table 1). When compared to the initial composition of dry components, this shows a relative increase in the binder fraction and some minor dissolution of calcite that probably occurred during the washing of the sample in distilled water. Zeolite cements are commonly reported in natural reservoir sandstones and are indicative of high porosity and permeability preservation during diagenesis [44].

3.2 SEM and EDX

SEM images of rock fragments taken from the cured synthetic sandstone sample show that quartz grains are cemented by the geopolymer binder that consists mainly of zeolite NaP crystals with diameters between 15 and 25 µm as well as an amorphous Si-rich geopolymer phase (Fig. 3a, b). The binder is primarily located in between quartz grains and contains varying amounts of porosity, which explains the broad range of grey values observed in CT images for this phase (Fig. 3a, b). To determine its chemical composition, EDX spectra of different binder and quartz grain spots were collected (Table 2). Binder regions B1–B3 are composed of Na, Al, Si, K, Ca and O with traces of Mg detected in B1. Na, Al, Si and O can be related to the zeolite NaP. The traces of Mg and K are likely remnants of the muscovite that was introduced with the metakaolin precursor material. The low concentration of Ca observed across all spectra is considered to represent some local calcite dissolution that likely occurred during the curing of the sample under strong alkaline conditions or the washing in slightly acidic double-distilled water. Subsequently, this Ca was either incorporated in the geopolymer during

Table 1 Petrophysical properties and mineralogical composition of the synthetic sandstone plug

	Synthetic sandstone	Berea sandstone	Flechtingen sandstone
Φ_{water} (%)	22.8	13.1	5.8
Φ_{CT} (%)	12.6	12.3	6.7 ± 3.4[a]
K_{air} (md)	1610 ± 423	117 ± 49	2.9 ± 1.5[a]
K_{calc} (md)	463 ± 315	Not determined	1.3[a]
σ (MPa)	19.6	91.2	129.2
Average mineral contents (wt%)			
Quartz	84	88	64
Zeolite	6	–	–
Calcite	8	1	6
Illite/muscovite	< 1	3	13
Titanium and iron oxides	< 1	< 1	< 1
Kaolinite	–	2	–
Feldspars	–	6	16

Values for Berea and Flechtingen sandstone are provided for comparison

Φ porosity, K permeability, σ uniaxial compressive strength

[a]Data compiled from Heidsiek et al. [10], Jacob et al. [45] and Peltz et al. [12]

Fig. 3 **a** Low resolution secondary electron image of the synthetic sandstone. Binder is found in intergranular regions and shows varying degrees of porosity depending on the amount of pore-filling amorphous geopolymer. The locations of quartz (Qz1-3) and binder (B1-3) EDX spot analyses from Table 2 are marked by blue and yellow frames. **b + c** Close-up and selected EDX maps showing the distribution of zeolite NaP and amorphous geopolymer
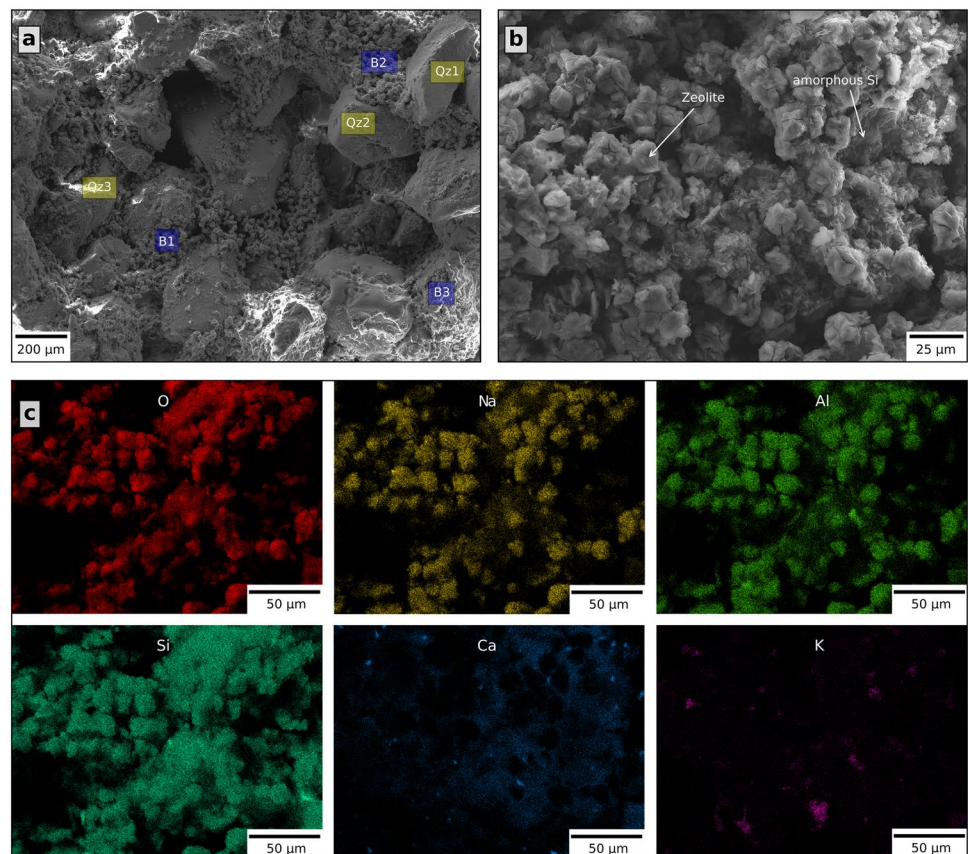
Table 2 Results of EDX spot measurements

	Na	Mg	Al	Si	K	Ca	O
Qz1	0.6	–	0.5	45.2	–	1.2	52.6
Qz2	1.4	–	1.4	42.5	–	3.2	51.5
Qz3	1.3	–	2.0	41.9	–	3.4	51.4
B1	5.7	0.4	8.7	32.1	0.9	3.9	48.3
B2	8.6	–	10.1	29.3	0.9	4.0	47.1
B3	4.2	–	7.0	32.8	1.5	6.7	47.9

Locations of the spots are shown in Fig. 3. All values in weight%

the curing as indicated by areas in the mapping that correlate with Si, or reprecipitated as calcite during the drying, as shown by the peaks of Ca that do not correlate with Si but with O (Fig. 3c).

EDX mappings of a larger area were collected to determine the chemical variability of the binder (Fig. 3b, c). The visibly crystalline parts (Fig. 3b) that are formed by zeolite are composed of Na, Al, Si and O. In between these crystals, an amorphous phase can be observed, which is primarily composed of Si and Al and is likely the amorphous geopolymer. Thus, higher Si contents correspond to denser and geopolymer-rich binders as confirmed visually and chemically by comparing site B2 with B3 (Fig. 3a; Table 2).

3.3 Petrophysical properties

To compare the properties of the geopolymer-based synthetic sandstone plug to natural rock plugs of the same dimensions, air permeability K_{air}, uniaxial compressive strength σ and water displacement porosity Φ_{water} were also measured for a Berea sandstone specimen representing a porous siliciclastic reservoir rock and a Flechtingen sandstone (Upper Rotliegend, Parchim Formation) as an example for a compacted, tight sandstone (Fig. 1; Table 1).

The total porosity of the synthetic sandstone obtained from water uptake (22.8%) and from CT images (12.6%) is within the typical range reported for natural porous reservoir sandstones [9]. These porosity values indicate that a large proportion of pores cannot be resolved by CT, such as the small pores associated with the zeolite and the amorphous geopolymer binder phase. Axis connectivity of the segmented pore space exists in all spatial directions and is built-up by a single connecting pore cluster (Fig. 4a). The fluctuations of the porosity and the binder content between consecutive images are low, but an overall decrease can be observed for both parameters from top to bottom (Fig. 4b). This is accompanied by a slight increase in quartz content observed from top to bottom (Fig. 4b), which reflects some gravitational settling of quartz grains during the curing process. These variations are, however, minor when compared to that produced by

the sedimentary grading of sand grains common to water-deposited sands and lithified sandstones.

Other, more local heterogeneities exist at a scale of a few 100 μm in association with clustered binder-rich regions with low porosity (Fig. 4a). It is also noticeable that the mineral phases in the upper 100 slices show large fluctuations and an increased porosity that can be viewed as an artefact of the molding process. Two additional anomalies in binder content and porosity are recognised in the regions around slice #700 and #1000, which mark regions where material was placed on top of each other during the filling of the mold. Despite these irregularities and artefacts, the overall bulk sample can be considered to be homogeneous and shows a consistent pore structure.

The calculated pore and binder size distributions (Fig. 4c) correlate well with the observed internal framework structure. The total volume fraction of the binder is 22.1% and the diameter of the binder coating between individual grains ranges between 15.2 and 22.8 nm. In comparison, the pore size distribution detected from CT imaging is broader with a peak abundance at about 38 nm (Fig. 4c).

By adding calcite as the last component during the rock mixture preparation, most calcite grains were located in open pores making them accessible for invading fluids. The textures observed are therefore similar to late-diagenetic calcites formed in reservoir sandstones [46]. In addition, the distribution of calcite shows only minor variations in texture across the specimen. This reflects that the synthetic geopolymer sample is notably more homogenous than reported from natural samples.

To check the homogeneity of the sample quantitatively, the range of permeabilities across the sample was simulated by selecting 12 sub-volumes of 384^3 voxels from three different depths and conducting separate numerical simulations (Fig. 4d). Four laterally located non-overlapping volumes were taken from the top, from below the highly porous zone at a depth of 128 voxel and from a depth of 512 voxels, respectively. All depths are related to the top face of the cubic domain. The measured and calculated permeability range shows a large fluctuation

Fig. 4 **a** 3D rendering showing the processed CT image, the machine-learning based segmentation and the voxel-rendering of the connected pore space. **b** Slice-wise area distribution of the segmented phases showing a slight increase in quartz content from top to bottom. The first 100 slices are characterised by an increased porosity and solid contents indicating lower compaction at the top. **c** The calculated pore and binder size distributions indicate that the binder primarily occupies narrower intergranular regions. **d** Porosity-permeability relationship for 12 selected sub-volumes
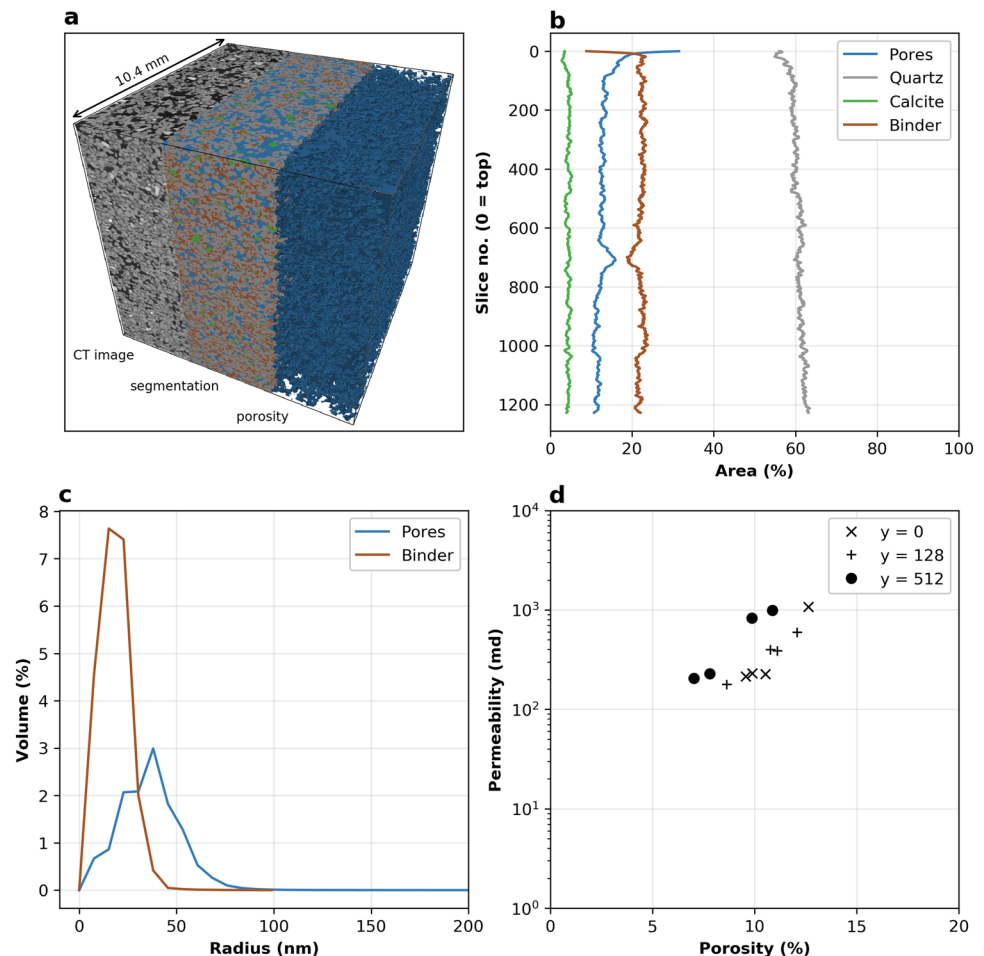
($K_{air} = 1610 \pm 423$ md, $K_{calc} = 463 \pm 315$ md) attributable to the low degree of compaction in the top area and varying degrees of pore connectivity at the simulated scale. It was observed that the connected porosity of sub-volumes from a depth of 512 voxels was 2–3% lower but the permeability values were within the same range as those observed for sub-volumes closer to the top. This indicates that the heterogeneity of connectivity of the pore space and flow paths was similar throughout the entire sample volume. Thus, the comparatively small sub-volumes of 384^3 voxels may not capture the representative elementary volume (REV) size of the sample. However, this issue is widely known when attempting to determine the permeability of natural sandstones by modelling [47] and deviations by a factor of 2 are generally expected for smaller volumes compared to the larger samples of the same material [48]. Although values fluctuated considerably, the permeabilities of the synthetic sandstone are up to 3 orders of magnitude higher than those observed in the natural samples (Table 1), which is favourable for conducting flow-through experiments [15].

The compressive strength of 19.6 MPa measured on the synthetic sandstone was significantly lower than that determined for the Berea (91.6 MPa) and Flechtingen (129.2 MPa) sandstones (Table 1). This low strength is attributed to insufficient hardening of the binder as evident from the remains of some amorphous geopolymer detected in the specimen. Increased hardening and therefore higher compressive strength may be achieved by various factors. (1) The presence of amorphous Si-rich geopolymer indicates an excess of sodium silicate solution in the starting materials. Thus, adjusting the molar ratios of the starting materials to zeolite NaP should lead to a more complete conversion of the educts, while reducing the likely mechanically weaker amorphous content. (2) Prolonged thermal curing of the geopolymer and/or applying a compressional force during the hardening stage may further increase the compressive strength. (3) The China clay utilised in the present study contains small amounts of muscovite, which was used to determine its suitability for particle migration studies. However, due to the intensive grinding, particle sizes became too small to be observed within the framework of this sample. Hence,
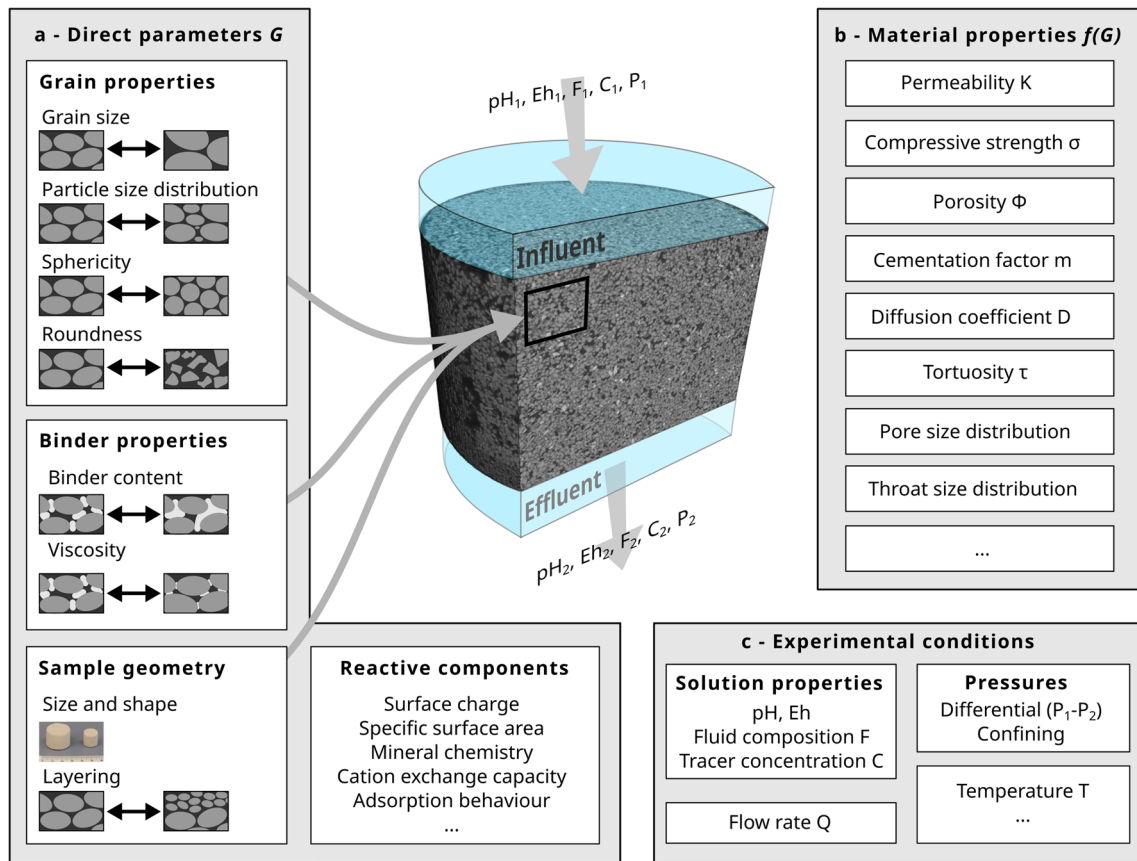
Fig. 5 Overview of parameters that can be adapted and material properties that can be constrained and investigated by flow-through experimentation of geopolymer-cemented synthetic sandstone. **a** Direct parameters G refer to properties that can be adjusted when preparing the sample. **b** Material properties that are a function of direct parameters. **c** Examples of experimental conditions that can be monitored or adjusted in flow-through experiments

adding more suitable particles separately that can be imagined for this purpose is recommended. Furthermore, the kaolinite could be replaced by a more disordered variety with smaller initial particle sizes and larger specific surface areas (possibly KGa2), as these are known to dissolve faster in alkaline environments [49].

3.4 Suitability for advancing experimental studies

Geopolymer-cemented synthetic sandstones containing thermally sensitive minerals have the potential of advancing experimental studies by providing more homogeneous solid materials that can be easily adapted to constrain specific reservoir rock parameters. Thus, these materials are considered to provide better analogues for reservoir rocks than synthetic rocks cured at high temperatures [17, 18, 20] or unconsolidated and consolidated sands [50, 51]. Examples of the direct parameters G that can be adjusted when preparing the samples, and the main corresponding reservoir-relevant properties f(G) that can be constrained,

are summarised in Fig. 5. These, and additional parameters, are required by available reactive transport models and can be provided for verifying these by improved controlled experimentation [14, 52–54].

In this proof-of-concept study, specimens were prepared with the focus of adding a matrix calcite (8 wt%) to a highly porous framework during the final stage of mixing as an analogue to a carbonate-cemented sandstone. Similar synthetic rocks can be constructed using other temperature-sensitive minerals, such as clay minerals (e.g. kaolinites, illites, smectites, chlorites) as well as various zeolites (clinoptilolite, heulandite, erionite, mordenite, analcime) which are common to the matrix of reservoir sandstones [55, 56]. These mixtures can be used to study surface-related processes, such as adsorption, cation exchange and reactive transport that cannot be constrained when high-temperature curing procedures induce irreversible mineral alterations.

In addition to adapting mineral contents, various grain properties can be selected when preparing the mixtures that are important for studying porosity-permeability

relationships as well as controlling pore and throat size distributions and tortuosity (Fig. 5a). Basic properties that are easy to control are grain size, grain-size distribution, sphericity, roundness and surface properties [57]. Recent numerical simulations, for example, indicate that the degree of adhesion and surface roughness in porous rocks will determine whether or not small particles are mobilised at the sub-pore scale, leading to reservoir clogging [58].

A range of matrix parameters can also be controlled by adjusting the binder mixture. This is an important aspect in influencing the volume and distribution of the cement that controls porosity, permeability, diffusivity, compressive strength, as well as the rate of fluid flow (Fig. 5b, c). Combining variations in mineral content, grain and binder properties using synthetic geopolymer sandstones may also lead to improved studies relevant to inorganic and organic pollutants based on monitoring changes in the chemistry of the effluent (Fig. 5c).

Geopolymer-hardened sandstones can be prepared in range of sample sizes and shapes applying no or very low confining pressures. Thus, it is straightforward to produce highly porous synthetic sandstone using simple mineral assemblages that are often difficult to find in natural sample collections. Any inconsistencies in porosity produced at the top or bottom of the synthetic sample can be easily removed before experimentation and internal inconsistencies can be avoided by pouring the slurry into the mold as one continuous process.

4 Conclusion

This study demonstrated that homogenous synthetic sandstones can be prepared at low temperatures using geopolymer binder that have the potential to provide improved analogue materials for constraining experimental parameters that are difficult to attain from the study of natural heterogenous rocks. The low-temperature curing enables the incorporation of temperature-sensitive materials such as carbonates, zeolites or clay minerals that cannot be studied using conventional high-temperature hardening approaches. Although the maximum temperature in the present study did not exceed 130 °C, many geopolymer studies indicate that curing even at room temperature may be achievable if longer curing times are used.

The variety of parameters, such as grain and cement properties, sample geometry and mineralogical composition, that can be easily adapted during the sample preparation, allows adaption to attain specific experimental requirements. Thus, the use of synthetic geopolymer-cemented sandstones in flow-through experiments has the potential to provide needed benchmark materials and datasets for verifying reactive transport models from the pore to the Darcy scale. As some improvements in the specimen preparation are still required to reach compressive strengths equal to those of hard reservoir rocks, the material synthesised in this study is considered more useful for studying fluid-rock interactions than mechanical aspects.

Declarations

Competing interests The authors declare that they have no conflicts of interest.

References

1. Jackson RB et al (2001) Water in a changing World. Ecol Appl 11:1027–1045. https://doi.org/10.1890/1051-0761(2001)011[1027:WIACW]2.0.CO;2
2. Ozano K et al (2022) Groundwater: making the invisible visible. FCDO Briefing Pack on Water Governance, Finance and Climate Change, K4D Briefing Note, Brighton: Institute of Development Studies. https://doi.org/10.19088/K4D.2022.027

3. Haszeldine RS (2009) Carbon capture and storage: how green can black be? Science 325:1647–1652. https://doi.org/10.1126/science.1172246

4. Amid A et al (2016) Seasonal storage of hydrogen in a depleted natural gas reservoir. Int J Hydrog Energy 41:5549–5558. https://doi.org/10.1016/j.ijhydene.2016.02.036

5. Welsch B et al (2016) Characteristics of medium deep borehole thermal energy storage. Int J Energy Res 40:1855–1868. https://doi.org/10.1002/er.3570

6. Barbier E (2002) Geothermal energy technology and current status: an overview. Renew Sustain Energy Rev 6:3–65. https://doi.org/10.1016/S1364-0321(02)00002-3

7. Lesmes DP, Frye KM (2001) Influence of pore fluid chemistry on the complex conductivity and induced polarization responses of Berea sandstone. J Geophys Res 106:4079–4090. https://doi.org/10.1029/2000JB900392

8. Stück H et al (2013) Petrographical and petrophysical properties of sandstones: statistical analysis as an approach to predict material behaviour and construction suitability. Environ Earth Sci 69:1299–1332. https://doi.org/10.1007/s12665-012-2008-1

9. Worden RH, Burley SD (2003) Sandstone diagenesis: the evolution of sand to stone. In: Burley SD, Worden RH (eds) Sandstone diagenesis. Blackwell Publishing Ltd, Oxford, pp 1–44. https://doi.org/10.1002/9781444304459.ch

10. Heidsiek M et al (2020) Small-scale diagenetic facies heterogeneity controls porosity and permeability pattern in reservoir sandstones. Environ Earth Sci 79:1–14. https://doi.org/10.1007/s12665-020-09168-z

11. Noh JH, Boles JR (1993) Origin of Zeolite cements in the Miocene Sandstones, North Tejon Oil Fields, California. SEPM JSR, vol 63. https://doi.org/10.1306/D4267AD2-2B26-11D7-8648000102C1865D

12. Peltz M et al (2022) A FIB-SEM study of Illite morphology in Aeolian Rotliegend Sandstones: implications for understanding the petrophysical properties of reservoir rocks. Clays Clay Miner 70:84–105. https://doi.org/10.1007/s42860-022-00174-9

13. Chagneau A et al (2015) Mineral precipitation-induced porosity reduction and its effect on transport parameters in diffusion-controlled porous media. Geochem Trans 16:13. https://doi.org/10.1186/s12932-015-0027-z

14. Iliev O (2017) On the pore-scale modeling and simulation of reactive transport in 3D geometries. Math Modelling Anal 22:671–694. https://doi.org/10.3846/13926292.2017.1356759

15. Hale S et al (2022) Upscaling calcite dissolution rates in a tight reservoir sandstone. Environ Earth Sci 81(11):303. https://doi.org/10.1007/s12665-022-10399-5

16. Abd AS, Abushaikha AS (2021) Reactive transport in porous media: a review of recent mathematical efforts in modeling geochemical reactions in petroleum subsurface reservoirs. SN Appl Sci 3:1–28. https://doi.org/10.1007/s42452-021-04396-9

17. Rathore JS et al (1995) P- and S-wave anisotropy of a synthetic sandstone with controlled crack geometry. Geophys Prospect 43:711–728. https://doi.org/10.1111/j.1365-2478.1995.tb00276.x

18. den Brok SW et al (1997) Preparation of synthetic sandstones with variable cementation for studying the physical properties of granular rocks. Comptes Rendus de l'Académie des Sci Ser IIA Earth Planet Sci 325:487–492. https://doi.org/10.1016/S1251-8050(97)89866-7

19. Turner ML et al (2004) Three-dimensional imaging of multiphase flow in porous media. Physica A 339:166–172. https://doi.org/10.1016/j.physa.2004.03.059

20. Tillotson P et al (2012) Experimental verification of the fracture density and shear-wave splitting relationship using synthetic silica cemented sandstones with a controlled fracture geometry. Geophys Prospect 60:516–525. https://doi.org/10.1111/j.1365-2478.2011.01021.x

21. Patsoukis Dimou A et al (2022) Benchmarking the viability of 3D printed micromodels for single phase flow using particle image velocimetry and direct numerical simulations. Transp Porous Med 141:279–294. https://doi.org/10.1007/s11242-021-01718-8

22. Al-Homadhi ES (2002) Artificial sandstone cores production with a wide range of petrophysical properties. J King Saud Univ-Eng Sci 14:95–117. https://doi.org/10.1016/S1018-3639(18)30747-5

23. Kozhagulova A et al (2021) An integrated laboratory experiment of realistic diagenesis, perforation and sand production using a large artificial sandstone specimen. J Rock Mech Geotech Eng 13:154–166. https://doi.org/10.1016/j.jrmge.2020.09.004

24. Subasri R, Näfe H (2008) Phase evolution on heat treatment of sodium silicate water glass. J Non-cryst Solids 354:896–900. https://doi.org/10.1016/j.jnoncrysol.2007.08.037

25. Duxson P et al (2007) Geopolymer technology: the current state of the art. J Mater Sci 42:2917–2933. https://doi.org/10.1007/s10853-006-0637-z

26. Davidovits J (1991) Geopolymers. J Therm Anal 37:1633–1656. https://doi.org/10.1007/BF01912193

27. Weng L, Sagoe-Crentsil K (2007) Dissolution processes, hydrolysis and condensation reactions during geopolymer synthesis: Part I—low Si/Al ratio systems. J Mater Sci 42:2997–3006. https://doi.org/10.1007/s10853-006-0820-2

28. Muñiz-Villarreal MS et al (2011) The effect of temperature on the geopolymerization process of a metakaolin-based geopolymer. Mater Lett 65:995–998. https://doi.org/10.1016/j.matlet.2010.12.049

29. Albidah A et al (2021) Characteristics of metakaolin-based geopolymer concrete for different mix design parameters. J Mater Res Technol 10:84–98. https://doi.org/10.1016/j.jmrt.2020.11.104

30. Doebelin N, Kleeberg R (2015) Profex: a graphical user interface for the Rietveld refinement program BGMN. J Appl Crystallogr 48:1573–1580. https://doi.org/10.1107/S1600576715014685

31. Cyr M et al (2012) Use of metakaolin to stabilize sewage sludge ash and municipal solid waste incineration fly ash in cement-based materials. J Hazard Mater 243:193–203. https://doi.org/10.1016/j.jhazmat.2012.10.019

32. Li J et al (2022) Longitudinal single-sided NMR study: silica-to-alumina ratio changes the reaction mechanism of geopolymer. Cem Concr Res 160:106921. https://doi.org/10.1016/j.cemconres.2022.106921

33. Singh PS et al (2005) Geopolymer formation processes at room temperature studied by 29Si and 27Al MAS-NMR. Mater Sci Eng A 396:392–402. https://doi.org/10.1016/j.msea.2005.02.002

34. Park S, Pour-Ghaz M (2018) What is the role of water in the geopolymerization of metakaolin? Constr Build Mater 182:360–370. https://doi.org/10.1016/j.conbuildmat.2018.06.073

35. Hale S et al (2020) Method comparison to determine hydraulic apertures of natural fractures. Rock Mech Rock Eng 53:1467–1476. https://doi.org/10.1007/s00603-019-01966-7

36. Hale S, Blum P (2022) Bestimmung der hydraulischen Durchlässigkeiten eines Sandsteins mithilfe eines Luftpermeameters. Grundwasser - Zeitschrift der Fachsektion Hydrogeologie 27:57–65. https://doi.org/10.1007/s00767-021-00504-z

37. Dietel J et al (2017) The importance of specific surface area in the geopolymerization of heated illitic clay. Appl Clay Sci 139:99–107. https://doi.org/10.1016/j.clay.2017.01.001

38. Damon J et al (2022) Mechanical surface treatment of EBM Ti6Al4V components: effects of the resulting surface layer state on fatigue mechanisms and service life. Mater Sci Eng A 849:143422. https://doi.org/10.1016/j.msea.2022.143422

39. Englert L et al (2020) Investigations on printing path dependent properties of additively manufactured samples using micro

computed tomography. RPJ 26:1603–1614. https://doi.org/10.1108/RPJ-07-2019-0200

40. Berg S et al (2019) ilastik: interactive machine learning for (bio) image analysis. Nat Methods 16:1226–1232. https://doi.org/10.1038/s41592-019-0582-9

41. Münch B, Holzer L (2008) Contradicting geometrical concepts in pore size analysis attained with Electron Microscopy and Mercury Intrusion. J Am Ceram Soc 91:4059–4067. https://doi.org/10.1111/j.1551-2916.2008.02736.x

42. OPENCFD (2016) OpenFOAM, the open source cfd toolbox. User Guide

43. Hildebrando EA et al (2014) Synthesis and characterization of zeolite NaP using kaolin waste as a source of silicon and aluminum. Mater Res 17:174–179. https://doi.org/10.1590/S1516-14392014005000035

44. Weibel R et al (2019) Thermogenetic degradation of early zeolite cement: an important process for generating anomalously high porosity and permeability in deeply buried sandstone reservoirs? Mar Pet Geol 103:620–645. https://doi.org/10.1016/j.marpetgeo.2019.02.006

45. Jacob A et al (2021) Simulating permeability reduction by clay mineral nanopores in a tight sandstone by combining computer X-ray microtomography and focussed ion beam scanning electron microscopy imaging. Solid Earth 12:1–14. https://doi.org/10.5194/se-12-1-2021

46. Morad S et al (2010) The impact of diagenesis on the heterogeneity of sandstone reservoirs: a review of the role of depositional facies and sequence stratigraphy. Bulletin 94:1267–1309. https://doi.org/10.1306/04211009178

47. Arns CH et al (2005) Cross-property correlations and permeability estimation in sandstone. Phys Rev E 72:46304. https://doi.org/10.1103/PhysRevE.72.046304

48. Blunt MJ (2017) Multiphase flow in permeable media. Cambridge University Press, Cambridge

49. Werling N et al (2022) Solubility of Calcined Kaolinite, Montmorillonite, and Illite in high molar NaOH and suitability as precursors for geopolymers. Clays Clay Miner 70:270–289. https://doi.org/10.1007/s42860-022-00185-6

50. Walton IC et al (2002) Perforating unconsolidated sands: an experimental and theoretical investigation. SPE Drilling Completion 17:141–150. https://doi.org/10.2118/79041-PA

51. Dehghani A et al (2013) Experimental investigation of sand consolidation techniques: resin injection and in-situ combustion. IJOGCT 6:689. https://doi.org/10.1504/IJOGCT.2013.056738

52. Maes J, Menke HP (2021) GeoChemFoam: direct modelling of multiphase reactive transport in real pore geometries with equilibrium reactions. Transp Porous Med 139:271–299. https://doi.org/10.1007/s11242-021-01661-8

53. Molins S et al (2021) Simulation of mineral dissolution at the pore scale with evolving fluid-solid interfaces: review of approaches and benchmark problem set. Comput Geosci 25:1285–1318. https://doi.org/10.1007/s10596-019-09903-x

54. Schabernack J, Fischer C (2022) Improved kinetics for mineral dissolution reactions in pore-scale reactive transport modeling. Geochim Cosmochim Acta 334:99–118. https://doi.org/10.1016/j.gca.2022.08.003

55. Reed JK, Gipson Jr M, Vass D (1993) Hydrocarbon potential of sandstone reservoirs in the East Slovakian basin, part 2: zeolites and clay minerals. J Pet Geol 16:223–236. https://doi.org/10.1111/j.1747-5457.1993.tb00108.x

56. Wilson MJ et al (2014) The influence of individual clay minerals on formation damage of reservoir sandstones: a critical review with some new insights. Clay Min 49:147–164. https://doi.org/10.1180/claymin.2014.049.2.02

57. Kong H et al (2020) The variation of grain size distribution in rock granular material in seepage process considering the mechanical-hydrological-chemical coupling effect: an experimental research. R Soc Open Sci 7:190590. https://doi.org/10.1098/rsos.190590

58. Sadeghnejad S et al (2022) Numerical simulation of particle retention mechanisms at the sub-pore scale. Transp Porous Med 145(1):127–151. https://doi.org/10.1007/s11242-022-01843-y